

Correction of Concomitant Magnetic Field-Induced Image Artifacts in Nonaxial Echo-Planar Imaging

Yiping P. Du,^{1*} Xiaohong Joe Zhou,² and Matt A. Bernstein³

Echo-planar images acquired in nonaxial planes are often distorted. Such image distortion has limited the applications of the echo-planar imaging (EPI) technique. In this article, it is demonstrated that a considerable amount of the distortion is caused by the higher-order magnetic field concomitant with the linear magnetic field gradient, or the concomitant magnetic field. The image distortion caused by the concomitant magnetic field is more prominent when a higher gradient amplitude is used for readout. It is also shown that the concomitant magnetic field can cause ghosting and blurring. A theoretical analysis is performed for the concomitant field effect in nonaxial EPI images. A point-by-point (or line-by-line) phase correction algorithm is developed to correct the image distortion, ghosting, and blurring. A postreconstruction processing algorithm is also developed to correct image distortion with much higher computational efficiency. Experimental results show that both correction methods effectively reduce the image distortion in coronal or sagittal images. Magn Reson Med 48:509–515, 2002. © 2002 Wiley-Liss, Inc.

Key words: concomitant magnetic field; Maxwell field; echo-planar imaging; phase correction.

Echo-planar imaging (EPI) (1) is one of the ultrafast MR imaging techniques. EPI, however, can suffer from severe image distortion in nonaxial planes due to the concomitant field effect, or Maxwell field effect (2–5). B_0 inhomogeneity (6), which is caused by both the susceptibility effect and the field inhomogeneity of the magnet, can also cause image distortion. Image distortion is one of the factors that have slowed the adoption of the EPI technique for routine clinical use. The sensitivity of EPI to B_0 inhomogeneity is due to a low bandwidth in the phase-encoding direction. The low bandwidth in the phase-encoding direction also makes EPI prone to the concomitant field effect. Because the bandwidth is much lower in the phase-encoding direction than in the frequency-encoding direction, the image distortion caused by B_0 inhomogeneity and the concomitant magnetic field is primarily along the phase-encoding direction.

Recently, high-performance gradient systems with higher gradient amplitude (e.g., 40 mT/m) and higher slew-rate (e.g., 150 T/m/s) have become commercially available for advanced imaging applications. The increased gradient amplitude and slew-rate were designed to improve the overall image quality of EPI by reducing the echo spacing and imaging time (7). When a high readout amplitude and a high slew-rate are used the image distortion caused by B_0 inhomogeneity is reduced because of the shortened echo spacing. With the increased gradient amplitude, however, EPI and other imaging sequences experience more severe concomitant magnetic field-related artifacts (8–11). In an MR imager with a high performance gradient system, the compensation of the concomitant field effect becomes more important.

In axial EPI, the concomitant magnetic field causes image shift and signal fall-off (11). The image distortion in nonaxial EPI due to the concomitant field effect has been demonstrated by Weisskoff et al. (5). However, the methods for correcting this image distortion remain to be explored. In this article, we theoretically analyze the concomitant magnetic field-induced artifacts in nonaxial EPI images. We develop a phase correction algorithm that eliminates the image distortion, along with the correction of minor ghosting and blurring, due to the concomitant magnetic field. We also develop an alternative postreconstruction processing algorithm to correct for image distortion.

THEORY

Concomitant Magnetic Field

In the absence of time varying electric field and electric current, the magnetic field in free space is governed by the following Maxwell's equations:

$$\begin{aligned}\vec{\nabla} \cdot \vec{B} &= 0, \\ \vec{\nabla} \times \vec{B} &= \vec{0}.\end{aligned}\quad [1-2]$$

The amplitude of the magnetic field is:

$$B = \sqrt{B_x^2 + B_y^2 + B_z^2}, \quad [3]$$

where B_x , B_y , and B_z are the three orthogonal components of the magnetic field. Using Eqs. [1] and [2], Eq. [3] can be expanded in a Taylor's series (8):

$$\begin{aligned}B &= B_0 + G_x x + G_y y + G_z z + \frac{(G_x^2 + G_y^2)z^2}{2B_0} - \frac{G_y G_z yz}{2B_0} \\ &\quad - \frac{G_x G_z xz}{2B_0} + \frac{G_x^2 x^2}{8B_0} + \frac{G_z^2 y^2}{8B_0} + \text{higher order terms},\end{aligned}\quad [4]$$

¹Department of Psychiatry and Radiology, University of Colorado Health Sciences Center, Denver, Colorado.

²Department of Diagnostic Radiology, M.D. Anderson Cancer Center, Houston, Texas.

³Mayo Clinic and Foundation, Rochester, Minnesota.

A major part of this study was conducted when the authors were the employees of General Electric-Medical Systems, Milwaukee, Wisconsin.

Part of this article was presented at the 6th Annual Meeting of the International Society of Magnetic Resonance in Medicine, Sydney, Australia, 1998.

*Correspondence to: Yiping P. Du, Ph.D., Department of Radiology, Box C-278, University of Colorado Health Sciences Center, 4200 E. 9th Avenue, Denver, CO 80262. E-mail: Yiping.du@UCHSC.edu

Received 8 January 2002; revised 26 March 2002; accepted 14 May 2002.

DOI 10.1002/mrm.10249

Published online in Wiley InterScience (www.interscience.wiley.com).

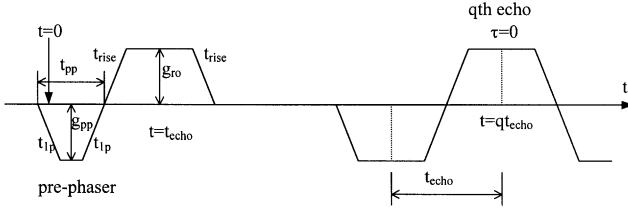


FIG. 1. The gradient waveforms of the readout train in EPI. The readout gradient amplitude is g_{ro} . The time interval between two consecutive echoes is t_{echo} . The center of the first echo is at $t = t_{echo}$. The area of the prephaser is equal to the area of one-half of the readout lobe. Depending on its amplitude, the concomitant field phase generated by the prephaser can differ from that generated by one-half of the readout lobe.

where G_x , G_y , and G_z are gradients along the x, y, and z directions, respectively. Note that x, y, and z are the coordinates in a magnet-based reference frame. In Eq. [4], the z-direction is defined as the direction of the main field B_0 . The $1/B_0$ and higher-order terms are called concomitant gradient terms and comprise the concomitant magnetic field. In this article, we only discuss the concomitant field effect corresponding to the $1/B_0$ order terms because the higher-order terms are usually substantially smaller.

Concomitant magnetic field-induced EPI artifacts are mainly caused by the readout gradient waveform. The concomitant magnetic field generated by the gradient pulses prior to the readout train induces a stationary phase variation in a complex image, but it does not affect the magnitude image. Although we only discuss the case of coronal images in this article, the case of sagittal images is analogous and can be analyzed similarly.

According to Eq. [4], the concomitant magnetic field depends on whether the readout is along the z-direction or the x-direction. For example, when the readout is along the x-direction and the phase-encoding is along the z-direction, the concomitant magnetic field for a coronal slice at $y = y_0$ is:

$$B_C = \frac{G_{ro}^2 z^2}{2B_0} + \frac{G_{pe}^2 (x^2 + y_0^2)}{8B_0}, \quad [5]$$

where G_{ro} and G_{pe} are the gradient amplitudes for readout and phase-encoding, respectively. With exchange between the readout and phase-encoding directions, the concomitant magnetic field is:

$$B_C = \frac{G_{ro}^2 (x^2 + y_0^2)}{8B_0} + \frac{G_{pe}^2 z^2}{2B_0}. \quad [6]$$

The concomitant field coefficient in Eq. [5] is four times larger than the concomitant field coefficient in Eq. [6] for an iso-center slice (i.e., $y_0 = 0$), when the concomitant magnetic field induced by the dephaser and phase blips (i.e., the second term in Eqs. [5] and [6]) is negligible.

In EPI, the k -space data are acquired using a series of phase-encoded bipolar readout gradient lobes (see Fig. 1). The concomitant magnetic field generated by the readout

and phase-encoding gradient waveform creates a time-varying phase, which we call the concomitant field phase:

$$\Phi_C(\tau, q, z) = \gamma \int_0^{q t_{echo} + \tau} B_C(z, t) dt$$

$$= \frac{\gamma}{2B_0} \int_0^{q t_{echo} + \tau} G_{ro}^2(t) z^2 dt + \sigma_{pp} z^2 + \sigma_{dp} z^2 + (q-1) \sigma_b z^2 \quad [7]$$

$$= \frac{\gamma}{2B_0} q z^2 \int_0^{t_{echo}} G_{ro}^2(t) dt + \frac{\gamma}{2B_0} z^2 \int_0^{\tau} g_{ro}^2 dt + \sigma_{pp} z^2 + \Phi_{pe} \quad [8]$$

$$= \frac{\gamma}{2B_0} g_{ro}^2 \left(t_{echo} - \frac{4}{3} t_{rise} \right) q z^2 + \frac{\gamma}{2B_0} g_{ro}^2 \tau z^2 + \sigma_{pp} z^2 + \Phi_{pe}, \quad [9]$$

where t_{echo} is the time interval between two consecutive echoes (i.e., echo spacing), t_{rise} is the ramp duration of the readout lobes, τ is a time variable originating from an echo center, $\sigma_{pp} z^2$ accounts for the difference in concomitant field phase generated by the first half of a readout lobe and by the prephaser, $\sigma_{dp} z^2$ is the concomitant field phase generated by the phase-encoding dephaser, $\sigma_b z^2$ is the concomitant field phase generated by a phase-encoding blip, q is echo index ($q = 1, \dots, N_{pe}$, where N_{pe} is the echo train length, and Φ_{pe} represents the phase-encoding terms. In Eqs. [8] and [9], the coefficient σ_{pp} is given by:

$$\sigma_{pp} = \frac{\gamma}{2B_0} g_{pp}^2 \left(t_{pp} - \frac{4}{3} t_{1p} \right) - \frac{\gamma}{4B_0} g_{ro}^2 \left(t_{echo} - \frac{4}{3} t_{rise} \right), \quad [10]$$

where g_{pp} , t_{pp} , and t_{1p} are indicated in Fig. 1. After flipping every other row of the sampled data in k -space for image reconstruction, we have:

$$\Phi_C(p, q) = \frac{\gamma}{2B_0} g_{ro}^2 \left(t_{echo} - \frac{4}{3} t_{rise} \right) q z^2 + (-1)^{q-1} \frac{\pi}{B_0} g_{ro} \left(p + \frac{1}{2} \right) \Delta k_{ro} z^2 + \sigma_{pp} z^2 + \Phi_{pe}. \quad [11]$$

In Eq. [11], the increment of k_{ro} corresponding to sampling interval, $\Delta\tau$, is:

$$\Delta k_{ro} = \frac{\gamma}{2\pi} g_{ro} \Delta\tau = \frac{1}{FOV_{ro}}, \quad [12]$$

where FOV_{ro} is the field-of-view in the readout direction, and p is the index for each sampled complex point along k_{ro} ($p = -N_{ro}/2, \dots, N_{ro}/2 - 1$ where N_{ro} is the dimension of the matrix in the readout direction). In single-shot EPI or multishot EPI with a small number of interleaves, the phase blips usually have a much lower gradient amplitude and shorter duration than the readout gradient lobes. For

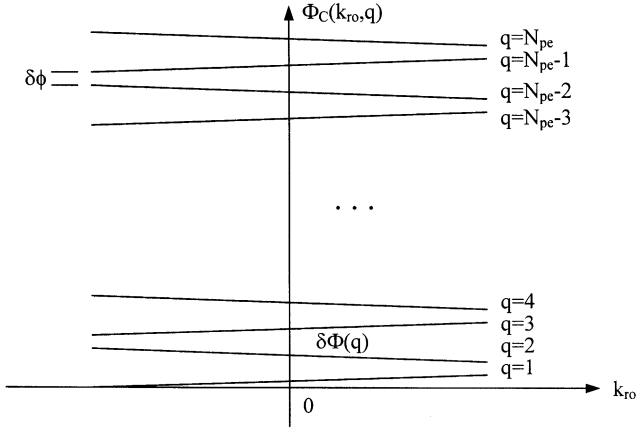


FIG. 2. The accumulation of concomitant field phase error from a point source in full-echo single-shot EPI with a readout gradient of alternating polarity, where q is the echo index. The slope of the concomitant field phase along k_{ro} is proportional to z^2 . The sign of the phase slope alternates for consecutive echoes. The phase increment, $\delta\phi$, is the concomitant field phase generated by the gradient ramps between two consecutive echoes.

simplicity, we ignore Φ_{pe} in Eq. [11] in the rest of this article.

The accumulation of concomitant field phase error from a point source in full-echo EPI, as given by Eq. [11], is depicted in Fig. 2. The slope of the concomitant field phase along k_{ro} is proportional to z^2 . The sign of the phase slope alternates for consecutive echoes. The phase increment, $\delta\phi$, is the concomitant field phase generated by the gradient ramps between two consecutive echoes.

From Eq. [11], the concomitant field phase linearly accumulates along the phase-encoding direction for any specific z value (see the first term in Eq. [11]). According to Fourier shift theorem (12):

$$\text{If } F^{-1}\{G(\omega)\} = g(t), \text{ then, } F^{-1}\{G(\omega)e^{i\alpha\omega}\} = g(t - \alpha), \quad [13]$$

where F^{-1} indicates inverse Fourier transform. This linear phase accumulation causes image pixel shift along the phase-encoding direction. Because the amount of pixel

shift depends on the value of z^2 , the concomitant field phase described by the first term in Eq. [11] causes image distortion in the phase-encoding direction.

From the second term in Eq. [11] the concomitant field phase also linearly accumulates during readout and the amount of accumulated phase again depends on the value of z^2 . With this additional linear phase, the image $\rho'(m, n)$ becomes (see Appendix A in Ref. 11):

$$\begin{aligned} \rho'(m, n) = & \frac{1}{2} \{ \rho(m + \beta_{ro}N_{ro}, n) + \rho(m - \beta_{ro}N_{ro}, n) \} \\ & + \frac{1}{2} \{ \rho(m + \beta_{ro}N_{ro}, n + N_{pe}/2) \\ & - \rho(m - \beta_{ro}N_{ro}, n + N_{pe}/2) \} \end{aligned} \quad [14]$$

where $\rho(m, n)$ is the object and $2\pi\beta_{ro}$ is the slope of the linear phase along the readout direction:

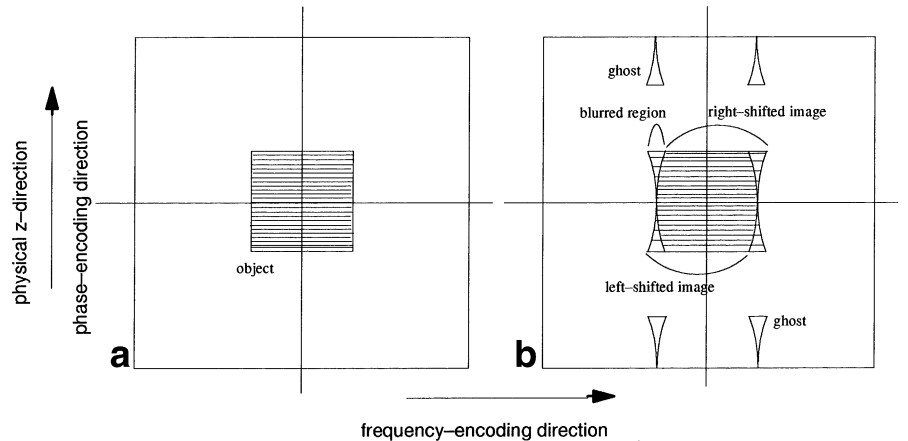
$$\beta_{ro} = \frac{1}{2B_0} \Delta k_{ro} g_{ro} z^2 = \frac{1}{2B_0} \frac{g_{ro}}{FOV_{ro}} z^2. \quad [15]$$

Note that β_{ro} is proportional to z^2 .

From Eq. [14], the first two terms form the image of the object and the last two terms form a Nyquist ghost. The image of the object is the average of two images shifted oppositely along the readout direction. The average of the two shifted images causes image blurring. The blurring increases as z^2 increases because (see Eq. [15]) β_{ro} is proportional to z^2 . From Eq. [14] we also see that the Nyquist ghost is the difference of the two shifted images, with a displacement of $FOV/2$ in the phase-encoding direction (see Fig. 3). The amount of ghosting and image blurring is usually not severe with the imaging parameters commonly used. In the example shown later in Fig. 5 where $B_0 = 1.5$ T and $g_{ro} = 21.31$ mT/m, the displacements along the readout direction in each of the shifted image ($=\beta_{ro}N_{ro}\Delta x$) were 0.07 mm at $z = 10$ cm and 0.31 mm at the edge of FOV. The maximum pixel displacement at the edge of FOV was much smaller than the pixel size, which was 3.28 mm.

Equations [11] and [15] were derived for the coronal images with the frequency-encoding along the x-direction.

FIG. 3. The formation of image blurring and Nyquist ghosting due to the concomitant magnetic field. Only the effect along the frequency-encoding direction is shown. **a:** A schematic of a uniform square object. **b:** Image of the object is the summation of a left-shifted image and a right-shifted image. The amount of shift is proportional to z^2 . The Nyquist ghosting is the difference between these two shifted images, with an offset of $FOV/2$ along the phase-encoding direction.



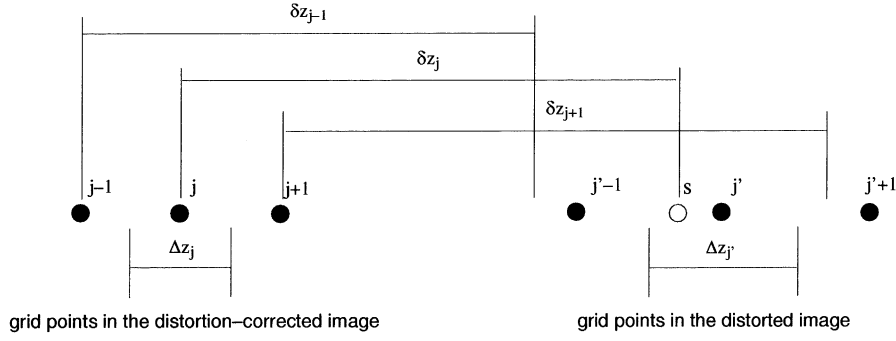


FIG. 4. Compression or dilation of pixel size along the phase-encoding direction due to the concomitant magnetic field. The solid dots denoted as $j'-1$, j' , and $j'+1$ represent the grid points in the distorted image. The solid dots denoted as $j-1$, j , and $j+1$ represent the grid points in the distortion-corrected image. A point j in the distortion-corrected image is shifted from a point s in the distorted image. In this case, the point s is located between two grid points, $j'-1$ and j' .

Similar equations can be analogously derived for coronal images with the readout along the z -direction.

Correction of Image Distortion, Ghosting, and Blurring via Phase Correction in Image Reconstruction

Using the theoretical analysis described in the previous section, image distortion, along with minor ghosting and blurring, can be largely eliminated by phase correction during image reconstruction. In the phase correction, the concomitant field phase is subtracted from the phase of the acquired k -space data before applying the inverse Fourier transform. In conventional applications of phase correction, the image artifacts caused by the phase errors are independent of spatial location in the image. In this study, however, the concomitant field phase is a function of both the spatial location in image and the location in k -space. In this situation, a spatially dependent phase-correction method is needed. In the method used in this study, we applied phase correction for one specific location at a time. This location can be a pixel, a line, or a small region. In the phase-corrected image, the pixels in the specific location were retained and the pixels in other locations were discarded. The phase correction was then repeated until all the locations in the image were reconstructed with phase correction. The phase-correction technique may not completely correct the concomitant field phase because 1) the phase correction in each repetition is exact only for specific spatial locations and the point spread function of a pixel is spatially extensive (i.e., a sinc function) (13); 2) the high-order terms in the concomitant field phase are not corrected.

Because the concomitant field phase is a function of the spatial coordinate $|z|$, the phase correction necessarily depends on each $|z|$ value. For a coronal image centered at $z = 0$ and with the phase-encoding in the z -direction, two rows in the reconstructed image with z and $-z$ spatial coordinates have the same concomitant field phase. The phase correction for this image needs to be repeated $N_{pe}/2$ times.

Correction of Image Distortion via Postreconstruction Processing

As an alternative to the phase-correction algorithm presented above, we also developed a postreconstruction processing algorithm for the correction of image distortion, not image ghosting. As discussed previously, the concomitant magnetic field causes image distortion along the

phase-encoding direction. The image distortion generated by the concomitant magnetic field can be corrected by shifting pixels in the reconstructed image, a similar approach that has been used in the correction of gradient nonuniformity (14) and B_0 inhomogeneity (15). The amount of pixel shift, δz , is a quadratic function of z :

$$\begin{aligned} \delta z &= \frac{\Phi_c(q) - \Phi_c(q-1)}{2\pi} FOV_{pe} \\ &= \frac{\gamma}{4\pi B_0} g_{ro}^2 \left(t_{echo} - \frac{4}{3} t_{rise} \right) FOV_{pe} z^2, \quad [16] \end{aligned}$$

where FOV_{pe} is the field-of-view along the phase-encoding direction, which is along the z -direction in this example.

In two-dimensional (2D) MR images, geometrical distortion can cause intensity variation because image intensity is proportional to the pixel area. This image intensity variation can be corrected when the variation of pixel area is known. According to Eq. [16], the amount of shift of a pixel depends on its $|z|$ value. In Fig. 4, three solid dots on the right represent three consecutive grid points in the distorted image; three solid dots on the left represent the corresponding grid points in the distortion-corrected image after correction. From Fig. 4 we can calculate the pixel dimension change after pixel shifting using a linear approximation:

$$\begin{aligned} \Delta z_j &= \frac{1}{2} [(z_{j+1} + \delta z_{j+1}) - (z_{j-1} + \delta z_{j-1})] \\ &= \Delta z_j + \frac{1}{2} (\delta z_{j+1} - \delta z_{j-1}), \quad [17] \end{aligned}$$

where:

$$\Delta z_j = \frac{1}{2} (z_{j+1} - z_{j-1}).$$

Then the intensity correction factor, Ω_j , for the intensity variation at the point j is:

$$\Omega_j = \frac{\Delta z_j}{\Delta z_j} = 1 + \frac{(\delta z_{j+1} - \delta z_{j-1})}{(z_{j+1} - z_{j-1})}. \quad [18]$$

Using Eq. [16], Eq. [18] can be rewritten as:

$$\Omega_j = \frac{\Delta z_{j'}}{\Delta z_j} = 1 + Cz_j, \quad [19]$$

where C is a constant given by:

$$C = \frac{\gamma}{2\pi B_0} g_{ro}^2 \left(t_{echo} - \frac{4}{3} t_{rise} \right) FOV_{pe}. \quad [20]$$

For a grid point in the corrected image, the corresponding point in the distorted image is not necessarily located at a grid point. For simplicity, we apply a linear interpolation to obtain the intensity value of this corresponding point using the intensities of its two nearest-neighboring grid points. Other interpolation algorithms may also be used. In Fig. 4, the point in the distorted image corresponding to the grid point j is located between the grid points $j'-1$ and j' . A linear interpolation is applied using the intensities at $j'-1$ and j' . In the case where the amount of shift causes a pixel to be relocated outside the FOV, this pixel is wrapped around to the other side of the FOV.

Although this postreconstruction processing algorithm is able to correct image distortion, it is unable to correct the ghosting and image blurring generated by the concomitant magnetic field as described by the second term of Eq. [11]. In contrast, the reconstruction-based phase correction algorithm can also correct ghosting and blurring generated by the concomitant magnetic field.

METHODS

Image Data Acquisition

The k -space data for a coronal image were acquired using a single-shot, spin-echo EPI sequence on a 1.5 T MR imager (General Electric—Medical Systems, Milwaukee, WI). The maximum gradient strength of the gradient system is 22 mT/m and its slew-rate is 120 T/m/s. A phantom filled with CuSO_4 solution was imaged with a standard birdcage body RF coil. The acquisition parameters were: FOV = 42 cm, TE = 105 ms, readout bandwidth = ± 192.3 kHz, slice thickness = 10 mm, and image matrix = 128×128 . The echo spacing was 832 μs . The readout amplitude was 21.31 mT/m and the ramp duration was 220 μs , which was de-rated for dB/dt purposes. The dataset was acquired with the phase-encoding direction parallel to the z -direction.

Implementation of the Correction for the Concomitant Field Effect

The phase-correction method presented in the Theory section was applied before the 2D inverse Fast Fourier transform (FFT) for each individual $|z|$ value. Two rows with z and $-z$ spatial coordinates were retained for the final image, while the rest of the image data were discarded. The phase correction and 2D inverse FFT were repeated 64 times for different $|z|$ values for the 128×128 image.

The postreconstruction algorithm was also implemented on the same workstation. The distorted image was reconstructed using a 2D inverse FFT. The postreconstruction algorithm included the following steps:

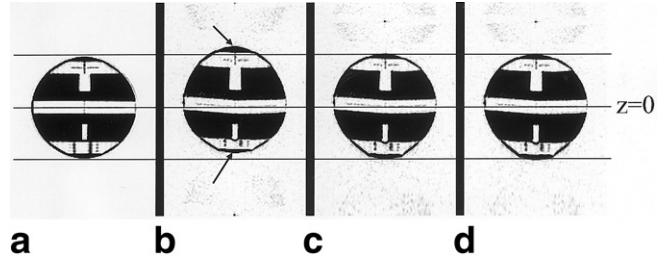


FIG. 5. Correction of the concomitant field effect in a coronal image with the phase-encoding along the z -direction: (a) a “distortion-free” reference coronal image acquired using a spin echo sequence, (b) a single-shot coronal EPI image without correction, (c) corrected using the phase correction algorithm, and (d) corrected using the postreconstruction algorithm. In **b**, both the top and bottom portions of the phantom, as indicated by the arrows, were distorted by more than 10 mm. Image distortion was substantially reduced in the corrected images. The effectiveness of the correction techniques is best demonstrated by the observation that both the top and bottom edges of the phantom in **c** and **d** are at approximately the same locations as in the reference image (i.e., in **a**), as marked by the upper and lower horizontal lines. The maximum pixel shift is approximately 13 mm at the top and bottom edges of the phantom. The shift in the central portion of the image (i.e., the pixels with a small z value) is very small. The remaining distortion in **c** and **d** is believed to be caused by B_0 inhomogeneity in the phantom.

- 1) Calculate the value of $|z|$ for each pixel in the distortion-corrected image, $I(i, j)$, which is initially blank. Calculate the amount of pixel shift along the phase-encoding direction, δz_j , using Eq. [16].

- 2) Find the corresponding point, s , in the distorted image. Obtain the intensity value of this corresponding point, $I'(i, s)$, where s is not necessarily an integer, by applying linear interpolation using the image intensities of its two nearest neighbors, $I'(i, j'-1)$ and $I'(i, j')$.

- 3) Calculate the intensity correction factor, Ω_j , for this point using Eqs. [19] and [20].

- 4) Obtain the intensity of the distortion-corrected image using the multiplication of Ω_j and $I'(i, s)$: $I(i, j) = \Omega_j I'(i, s)$.

- 5) Obtain the distortion-corrected image, $I(i, j)$, by repeating steps 1–4 for all the pixels.

Because all the pixels in a row in the corrected image have the same z value, the computational efficiency of the above algorithm can be improved by calculating δz_j and Ω_j only once for each row.

RESULTS

Figure 5a shows a reference coronal image acquired using a spin-echo sequence and Fig. 5b shows an EPI image of the same phantom acquired at the same location with the phase-encoding along the z -direction. In Fig. 5, the central horizontal line corresponds to $z = 0$. Note that the top part of the phantom image in Fig. 5b is dilated away from the line $z = 0$, while the bottom part of the phantom image is compressed towards it. The image distortion at the top and bottom of the phantom was approximately 13 mm (see arrows in Fig. 5b), in agreement with the theoretical prediction of 14.6 mm. It is noteworthy that the center of the image at $z = 0$ was not shifted compared to the image

shown in Fig. 5a. The theory of the concomitant magnetic field predicts that the amount of pixel shift (i.e., distortion) is proportional to z^2 . The observed feature of the distortion shown in Fig. 5b agrees with the theoretical prediction.

Figure 5c shows the postcorrection image obtained by applying the phase correction technique to the same acquired data as that used in Fig. 5b. The total computational time was approximately 45 sec using a Silicon Graphics Indy™ workstation (Silicon Graphics, Mountain View, CA). This computational time can be substantially reduced with faster computers, especially when a smaller image matrix (e.g., 64×64) is used. It was observed that most of the distortion was corrected with the phase correction technique. The effectiveness of distortion correction is best demonstrated by the observation that both the top and bottom edges in Fig. 5c are at approximately the same locations as in the “distortion-free” reference image (i.e., Fig. 5a), as marked by the upper and lower horizontal lines. In Fig. 5c the maximum pixel shift correction is approximately 13 mm at the top and bottom edges of the phantom. The shift in the central portion of the image (i.e., the pixels with a small z value) is very small. The remaining distortion is believed to be caused by B_0 inhomogeneity in the phantom.

The image corrected using the postreconstruction processing is shown in Fig. 5d. Before applying the pixel shift algorithm, the original image was zero-filled interpolated to reduce partial volume effect (16). The pixel shift algorithm provided the same distortion correction as the phase correction algorithm as shown in Fig. 5c. The computational time of this postreconstruction processing algorithm was about 0.21 sec for the interpolated 256×256 image using the same SGI workstation.

DISCUSSION

The concomitant field effect differs from the effects caused by B_0 inhomogeneity and susceptibility in many respects. First, the concomitant field is independent of imaging object, while the susceptibility effect is object-dependent. The image distortion and signal pile-up/reduction caused by B_0 inhomogeneity and susceptibility effect can be largely compensated by using a magnetic field map (6,15). The concomitant field effect can be fully characterized by the configuration of the scanner and the imaging parameters used in a scan. Second, the concomitant field phase is proportional to both the square of the gradient amplitude and the time duration in which the phase is accumulated, while the phase error caused by B_0 inhomogeneity and the susceptibility effect is proportional to the time duration only. As a result, increasing the readout bandwidth reduces the imaging artifacts caused by B_0 inhomogeneity and the susceptibility effect, but increases the imaging artifacts caused by the concomitant magnetic field.

The phase-correction approach is able to slightly reduce image ghosting. In another experiment (not shown), the peak ghost-to-image ratio was reduced from 5.0% to 4.3%. In many applications, however, the benefit of this reduction of ghost may not be well justified by the substantial increase of computational time. The postprocessing approach provides a computationally efficient and relatively simple alternative. The postprocessing approach can pos-

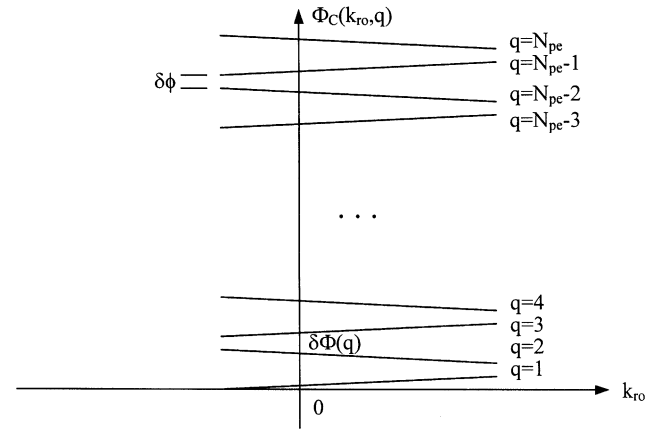


FIG. 6. The accumulation of concomitant field phase error from a point source in partial-echo EPI with alternating polarity of readout gradient, where q is the echo index. The alternating increment of the concomitant field phase at the echo center between two consecutive echoes, $\delta\Phi(q)$, causes additional image ghosting.

sibly be also combined with the correction of gradient nonuniformity (14) to further reduce computational time.

The concomitant field effect is increased at low B_0 field, as shown in Eq. [11]. For low field MR imagers, the correction of the concomitant field effect becomes more crucial. The combination of high readout gradient amplitude and low B_0 field will produce a considerably increased concomitant field effect.

The concomitant field effect will cause more ghosting in partial-echo EPI than in full-echo EPI. The extra amount of ghosting is induced by the alternating increment of the accumulated concomitant field phase between even and odd echoes at echo center (see Fig. 6).

In interleaved multishot EPI, the amount of image distortion caused by the concomitant field effect is reduced by a factor equal to the number of shots, as is the amount of image distortion caused by the B_0 inhomogeneity. With minor modifications, the phase correction algorithm can also be applied to EPI in which the data acquisition starts from $k_{pe} = 0$ and fills the k -space outward along the phase-encoding direction. The postreconstruction processing algorithm, however, is not applicable to these images.

In the case of double oblique images, the concomitant magnetic field causes a combination of image distortion and image shift along the phase-encoding direction. In this case, more than one $1/B_0$ concomitant gradient term in Eq. [4] cause image distortion, ghosting, and blurring. The concomitant field effect can be compensated with pixel-by-pixel phase correction. A region-by-region phase correction may provide a computationally efficient alternative. The postprocessing technique is a more practical approach in correcting distortion in double oblique images because of its higher computational efficiency.

For an axial image with a z -offset, z_0 , the amount of pixel shift caused by the concomitant magnetic field is a constant for all the pixels in the entire image. Therefore, the image distortion is reduced to image shift. In that special case, image shift can be corrected by adjusting the phase of receiver for different echoes during data acquisition, or by

displacing the image back to the original position after reconstruction (11).

In this study, we used a 2D inverse FFT to reconstruct images. For an image centered at $z = 0$, two rows in the distortion-corrected image have the same $|z|$ values and can be retained for the final image. Using this approach the 2D inverse FFT needs to be repeated $N_{pe}/2$ times. The computational time for image reconstruction can be further reduced by using a 1D inverse FFT. In this approach, a 1D inverse FFT is applied to each of the columns, a total of N_{ro} times. Then a 1D inverse FFT is applied to each of the two rows that have the same $|z|$ value. This process needs to be repeated $N_{pe}/2$ times (i.e., perform a 1D inverse FFT in a total number of $(N_{ro} + 2)N_{pe}/2$ times) in order to reconstruct the entire image. The computational time for a 2D inverse FFT of an array with $N_{ro}N_{pe}$ elements is:

$$T_{2-D} = \lambda N_{ro} N_{pe} \log_2(N_{ro} N_{pe}), \quad [21]$$

where λ is a factor which depends on the inverse FFT algorithm and on the computational power of the computer. The computational time for a 1D inverse FFT of an array with N_{ro} elements is:

$$T_{1-D} = \lambda N_{ro} \log_2(N_{ro}). \quad [22]$$

Based on Eqs. [21] and [22], the computational time for the phase-corrected image reconstruction using the 2D inverse Fourier transform approach is:

$$T_A = 0.5 \lambda N_{ro} N_{pe}^2 \log_2(N_{ro} N_{pe}), \quad [23]$$

and the computational time for phase-corrected image reconstruction using the 1D inverse Fourier transform approach is:

$$T_B = 0.5 \lambda (N_{ro} + 2) N_{ro} N_{pe} \log_2(N_{ro}). \quad [24]$$

Eqs. [23] and [24] show that the computational time using the 1D approach is approximately half ($= 1/2 + 1/N_{pe}$, when $N_{ro} = N_{pe}$) of the computational time using the 2D correction approach. For an image with $N \times N$ elements, for example, the reconstruction time is increased approximately by a factor of $N/4$ compared to a conventional reconstruction algorithm without the correction for concomitant field effect, assuming the computational time for phase subtraction prior to the FFT is negligible. For coronal or sagittal images with a z -offset, the symmetry about z does not apply for some of the rows and the computational time increases.

The computational time of the phase correction algorithm can be further reduced using a region-by-region approach. In this approach, the correction of concomitant field phase for z_0 is applied to the row that have a $|z|$ value in a range between $z_0 - \epsilon_0$ and $z_0 + \epsilon_0$. The region-by-region approach trades off accuracy for computational efficiency.

The phase correction algorithm and the postprocessing algorithm are not able to differentiate ghost from the object. Because Nyquist ghosts are displaced relative to the object, the ghost experiences a different amount of distortion correction compared to the object, as shown in Fig. 5c,d.

CONCLUSIONS

A considerable amount of image distortion in nonaxial echo-planar images can be generated by the concomitant magnetic field. The concomitant magnetic field can also cause a small amount of ghosting and blurring in nonaxial echo-planar images. The concomitant field effect increases with readout gradient amplitude and decreases with field strength. In this article, we showed that the concomitant magnetic field-induced image artifacts can be compensated using a point-by-point or line-by-line phase correction algorithm during image reconstruction. The concomitant magnetic field-induced image distortion can also be effectively corrected by using a postreconstruction processing algorithm.

ACKNOWLEDGMENTS

We thank Drs. G.H. Glover and N.J. Pelc of Stanford University for valuable discussion about the concomitant field effect. We also thank J.A. Derbyshire, J.K. Maier, and J.A. Polzin of General Electric–Medical Systems for helpful discussions and comments.

REFERENCES

1. Mansfield P. Multi-planar image formation using NMR spin echoes. *J Physics C* 1977;10:L55–58.
2. Norris DG. Phase errors in NMR images. In: Abstract Book: SMRM, 1985. p 1037.
3. Coxon R, Mansfield P. EPI spatial distortion in non-transverse planes. In: Abstract Book: SMRM, 1989. p 361.
4. Norris DG, Hutchinson JMS. Concomitant magnetic field gradients and their effects on imaging at low magnetic field strengths. *Magn Reson Imag* 1990;8:33–37.
5. Weisskoff RM, Cohen MS, Rzedzian RR. Nonaxial whole-body instant imaging. *Magn Reson Med* 1993;29:796–803.
6. Jezzard P, Balaban RS. Correction for geometric distortion in echo planar images from B_0 field variation. *Magn Reson Med* 1995;34:65–73.
7. Tang C, McVeigh ER, Zerhouni EA. Multi-shot EPI for improvement of myocardial tag contrast: comparison with segmented SPGR. *Magn Reson Med* 1995;33:443–447.
8. Bernstein MA, Zhou XJ, Polzin JA, King KF, Ganin A, Pelc N, Glover GH. Concomitant gradient terms in phase contrast MR: analysis and correction. *Magn Reson Med* 1998;39:300–308.
9. King KF, Ganin A, Zhou XJ, Bernstein MA. Effect of Maxwell fields in spiral scans. Concomitant gradient field effects in spiral scans. *Magn Reson Med* 1999;41:103–112.
10. Zhou XJ, Tan SG, Bernstein MA. Artifacts induced by concomitant magnetic field in fast spin echo imaging. *Magn Reson Med* 1998;40:582–591.
11. Zhou XJ, Du YP, Bernstein MA, Reynolds HG, Maier JK. Concomitant field induced artifacts in axial echo planar imaging. *Magn Reson Med* 1998;39:596–605.
12. Bracewell RN. The Fourier transform and its applications. New York: McGraw-Hill; 1978.
13. Parker DL, Du YP, Davis WL. The voxel sensitivity function in Fourier transform imaging: applications to magnetic resonance angiography. *Magn Reson Med* 1995;33:156–162.
14. Glover GH, Pelc NJ. Method for correction of image distortion due to gradient non-uniformity. US Patent 4,591,789; 1986.
15. Reber PJ, Wong EC, Buxton RB, Frank LR. Correction of off resonance-related distortion in echo-planar imaging using EPI-based field maps. *Magn Reson Med* 1998;39:328–330.
16. Du YP, Parker DL, Davis WL, Cao G. Reduction of partial-volume artifacts with zero-filled interpolation in three-dimensional MR angiography. *J Magn Reson Imag* 1994;4:733–741.